Near Surface Geophysics, 2014, **12**, 133-150 doi:10.3997/1873-0604.2013060

Geoelectrical monitoring: an innovative method to supplement landslide surveillance and early warning

Robert Supper[1], David Ottowitz[1], Birgit Jochum[1], Jung-Ho Kim[2], Alexander Römer[1], Ivo Baron[1], Stefan Pfeiler[1], Mario Lovisolo[3], Stefanie Gruber[1] and Filippo Vecchiotti[1]

[1] *Geological Survey of Austria, Neulinggasse 38, A-1030 Vienna, Austria*
[2] *Korea Institute of Geoscience and Mineral Resources (KIGAM), Korea*
[3] *C.S.G. S.r.l. – Centro Servizi di Geoingegneria, Italy*

Received October 2012, revision accepted September 2013

ABSTRACT

Permanent geoelectrical monitoring, using the GEOMON[4D] instrumentation in combination with high resolution displacement monitoring by means of the D.M.S. system, was performed at two active landslide areas: Ampflwang/Hausruck in Austria, and Bagnaschino in Italy. These sites are part of the Austrian geoelectrical monitoring network, which currently comprises six permanently monitored landslides in Europe. Within the observation intervals, several displacement events, triggered by intense precipitation, were monitored and analysed. All of these events were preceded by a decrease of electric resistivity. The application of an innovative 4D inversion algorithm made it possible to investigate the potential processes which led to the triggering of these events. We conclude that resistivity monitoring can significantly help in the investigation of the causes of landslide reactivation. Since the results also contribute to the extrapolation of local displacement monitoring data to a larger scale, resistivity monitoring can definitely support decision-finding in emergencies.

INTRODUCTION

Landslides are one of the major natural threats to human lives, settlements and infrastructure, causing enormous human suffering and property losses. The best way to restrain such high losses on property and lives is through effective land-use planning, based on a good knowledge of the landslide susceptibility, hazard and risk within specific areas as a part of mitigation (Chacón *et al.* 2006). However, due to several natural, historical or political reasons, this ideal approach is impossible to be implemented in many places. For example, many human settlements and infrastructure lines have already existed in landslide-prone areas or on dormant landslides decades before the establishment of detailed hazard zone maps. In most cases it is not possible to resettle people living in such areas. Consequently, it is the responsibility of stakeholders to guarantee a safe daily life of the people concerned.

The evaluation of actual hazards and the warning of people before a catastrophic event, require a good knowledge about the structure, dynamics, triggers, history and possible magnitude of such high-risk landslides. This knowledge can only be obtained via interpretation of data coming from investigations by different techniques, long-term continuous monitoring of deformation and triggering factors and by establishing early-warning systems/centres. The most commonly used early-warning parameters are pore pressure and displacement. However, recent research has shown that other parameters exist, which might give indications of impending triggering before an actual displacement is measurable.

The geoelectrical method (direct current DC) has recently been established as a routine geophysical method to investigate subsurface geometry and structural pattern of landslides in Europe (Mauritsch *et al*. 2000; Perrone 2001; Supper, Hübl and Jaritz 2002; Supper *et al.* 2008; Perrone *et al*. 2004, 2006; Meric *et al*. 2005; Jongmans and Garambois 2007; Baron and Supper 2010). With geoelectrical investigations it is possible to determine the distribution of the electrical resistivity of the subsurface. This parameter is a physical property of the substratum, which depends mainly on porosity, water saturation, conductivity of pore fluid and clay content (e.g., Archie 1942; Winsauer *et al*. 1952; Atkins and Smith 1961; Jackson, Taylor-Smith and Stanford 1978; Schlumberger 1987). Since most of the European landslide events are intimately related to precipitation and to the influence of underground water on slope stability (porewater pressure, change of water flow regime, saturation), observing temporal changes of the electric parameters aids interpretation of

* robert.supper@geologie.ac.at

subsurface processes (Chambers *et al*. 2010, 2011).

Nowadays, the permanent monitoring of temporal resistivity and self-potential changes starts to be used intensively for many different tasks. Jongmans and Garambois (2007) concluded that the development of 2D and 3D imaging techniques, as well as the installation of permanent geoelectrical monitoring systems, constitute major advances for future landslide reconnaissance; however, they also highlight the necessity to calibrate and correlate results with geological and geotechnical data. So far only some case studies of long-term geoelectrical monitoring experiments on landslides have been published (Supper *et al*. 2002, 2008, 2010; Bell *et al*. 2008; Chambers *et al*. 2009, 2010, 2011; Lebourg *et al*. 2010; Luongo *et al*. 2012). Only two authors (Chambers *et al*. 2010; Supper *et al*. 2012a) correlate the geoelectrical monitoring response with permanently monitored displacement data, whereas Wilkinson *et al*. (2010) have recovered array electrode movements directly from geoelectrical measurements during recent monitoring of mudflow events.

MAJOR COMPONENT OF THE MONITORING SYSTEM

The monitoring systems consist of geoelectrical monitoring equipment (GEOMON^{4D}) and an automatic inclinometer. Depending on the site and the available budget, other sensors are added on demand. From 2001, the GEOMON^{4D} instrument was developed specifically as a monitoring device at the Geological Survey of Austria (Supper, Römer and Jochum 2009). It offers an open architecture, allowing installation of any number of current or potential electrodes by adding parallel or serial boards. The principal characteristics are the high speed of data acquisition (approx. 3000 measurements/hour in single channel mode) and the recording of the full raw signal (usually 1000 samples per single configuration). The instrument operates in an automatic mode, performing a preselected chain of tasks each day, including several measurement jobs of self-potential and DC as well as maintenance, backup and shutdown routines. Moreover, Universal Mobile Telecommunications System (UMTS) data transfer was implemented. Therefore, software maintenance can be performed fully remote-controlled and data are sent automatically via email to the data processing centre each day. Since data can also be downloaded manually, immediate availability of information can be guaranteed in case of necessity.

However, the most innovative aspect comes from the fact that, for each single measurement, the raw signals (usually 1000 single samples for forward and backward current as well as for forward and backward potential with a sampling rate of 5000 values/second) are also recorded and saved. This opens the possibility for an optimized assessment of data quality and filtering, since only an analysis of raw data can provide information on data drift and noise content. In fact, each sample is statistically analysed on its signal-to-noise ratio and checked for linear or non-linear drifts. Furthermore, repeatability of the result (by dividing the sample into several subsamples and comparing the results), standard deviations for current and potential differences, as well as the differences of the injection current in forward and backward directions, are calculated. Based on these results, a data quality matrix is derived. Values not fulfilling the levels of a certain threshold matrix, whose values are determined for each site by analysing all samples for a one-month period, are then discarded (usually less than 10% of approximately 4000 measurements for a 93 electrode profile in gradient configuration). Omitting these data points usually does not confine subsurface coverage, but significantly

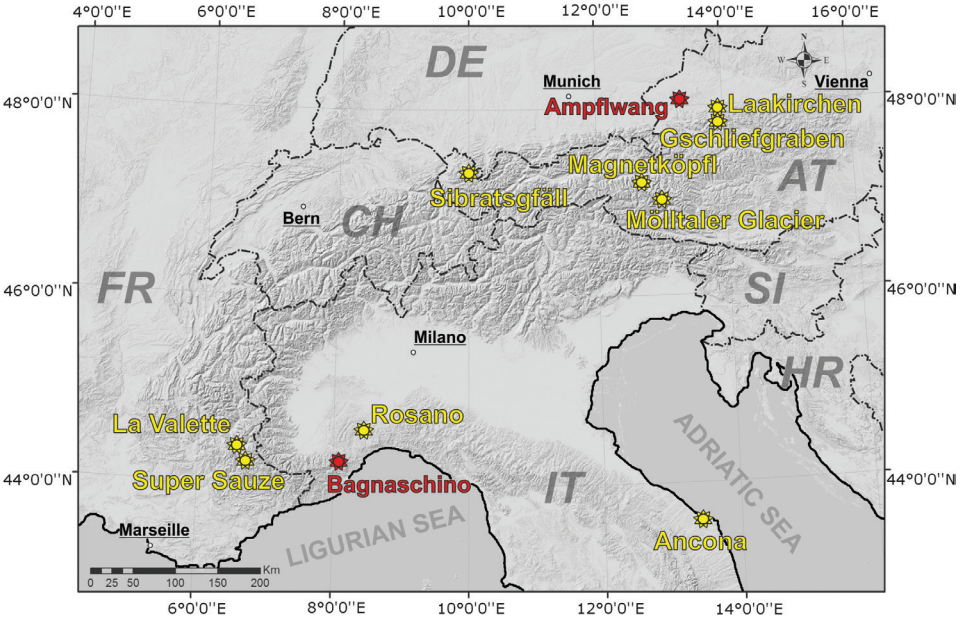

FIGURE 1
Location of the TEMPEL/SafeLand monitoring network (red: sites which are discussed in the present study).

enhances the reliability of the inversion results. In most cases the rejected values can be correlated with one or more single electrodes. Consequently, this analysis also gives advice for the on-site maintenance of the system. The quality matrix is also used in the inversion process for data weighting.

To correlate the results of the geoelectrical monitoring with the dynamic behaviour of a landslide, the availability of displacement data at a high sampling rate (at least hourly measurements) is an imperative. The necessity to monitor landslide stability conditions has encouraged the Centro Servizi di Geoingegneria (C.S.G.), Italy, to develop an innovative multiparametric monitoring system for stability, called D.M.S. (patent pending and trade mark C.S.G. S.r.l.). This device measures displacements in two or three directions (both horizontal and vertical at all the prefixed depths with high accuracy and precision), piezometric water levels and soil temperature, thus allowing a complex analysis of the dynamics of any landslide, e.g. deformation analysis, movements, depth of sliding surface or piezometric variations (Foglino, Lovisolo and Della Giusta 2006).

THE AUSTRIAN LANDSLIDE MONITORING NETWORK

In the frame of the EC funded FP7 project SafeLand, the Geological Survey of Austria, in cooperation with several different European partners, started to implement a European landslide monitoring test site network in 2007 (Supper *et al*. 2012a,b). The network was enlarged and further continued within the TEMPEL project. Currently, the active network (Fig. 1) consists of six landslide monitoring sites, two of them in Austria (Gschliefgraben, Laakirchen), one in France (La Valette), three in Italy (Bagnaschino, Ancona, Rosano), and one permafrost monitoring site in Austria (Magnetköpfl). Three other monitoring sites in Austria (Sibratsgfäll, Ampflwang-Hausruck, Mölltaler Glacier (permafrost site)) and one in France (Super-Sauze) were already closed, and the instrumentation was moved to other sites. In this paper the results of the test sites in Ampflwang and Bagnaschino (Fig. 1) are described in detail.

4D INVERSION ALGORITHM MINIMIZING LP NORM

The algorithm for inverting the monitoring data in this study originates from the 4D inversion algorithm (Kim *et al*. 2009). The inversion method involves two unique key concepts. Firstly, it simultaneously inverts the entire sets of monitoring data and correspondingly at once obtains a space-time model that is varying over the whole monitoring period. Secondly, it allows for the subsurface properties to continuously change in time during data acquisition of a geoelectrical section. To realize these concepts, the coordinate of every measured datum is defined in the space-time domain, i.e. in the 4D space. The material properties are also in the 4D domain. When the number of monitoring surveys is N, the inversion algorithms that do not adopt the 4D concepts seek N different static subsurface models by repeatedly (N times) inverting the N sets of monitoring data (e.g., Daily *et al*. 1992; Loke 1999; LaBrecque and Yang 2001; Oldenborger *et al*. 2007; Miller *et al*. 2008). In the 4D inversion, on the other hand, a single data vector that comprises the N different data sets is defined in the 4D, and a 4D model vector is calculated by inverting the 4D data vector. Defining the entire monitoring data and time-varying subsurface model in the space-time domain (4D space) allows us to introduce the regularizations not only in the space domain, but also in the time domain, so that inversion artefacts are effectively reduced (e.g., Hayley, Pidlisecky and Bentley 2011; Karaoulis, Kim and Tsourlos 2011a; Rucker, Finka and Loke 2011). The 4D inversion consists of three penalty terms: data misfit and two kinds of model roughness in the space and time domains. Particularly by minimizing the time-domain model roughness, we are able to obtain a reasonable 4D subsurface model which smoothly varies in time.

Kim *et al*. (2009) explain the key concepts in detail and demonstrate that the 4D approach can generate difference images with little inversion artefacts in a dye tracer flooding experiment even when the material properties are continuously changing during the acquisition of one geoelectrical section. The first concept, simultaneous inversion of multiple time-lapse data sets, has already been adopted in many studies. For example, Hayley, Pidlisecky and Bentley (2011) developed the simultaneous time-lapse inversion, a special case of the 4D inversion, where two sets of resistivity monitoring data are inverted. Comparing with other inversion algorithms, such as the ratio inversion (Daily *et al*. 1992), the cascade inversion (Miller *et al*. 2008) and the difference inversion (LaBrecque and Yang 2001), they showed that the 4D approach produced the best reconstruction of resistivity changes in the numerical example and in the field example. Karaoulis, Kim and Tsourlos (2011a) proposed the 4D active time constrained inversion, where the amount of time domain regularization is allowed to vary in space-time domain depending on the degree of spatial resistivity changes occurring among different monitoring stages. During the past 2 years, several studies have adopted the 3D spatial coordinate for the spatial dimension of the 4D inversion: for example, in the interpretation of complex resistivity (CR) monitoring data (Karaoulis *et al*. 2011b), for the monitoring of a simulated leak from an underground storage tank (Rucker, Finka and Loke 2011), and for the recovering of temporal changes of the subsurface resistivity due to rainwater infiltration as well as due to the migration of sodium cyanide solution (Loke, Dahlin and Rucker 2013). The 4D inversion concept has been extended to other material properties, such as CR monitoring (Karaoulis *et al*. 2011b), and joint inversion of cross well DC resistivity and seismic monitoring data (Karaoulis *et al*. 2012).

One of the special features of this inversion is to adopt the Lp norm minimization approach; any of the penalty terms, which are subjected to be minimized, can be selectively defined either in L1 or in L2 norm (Kim *et al*. 2010, 2012, 2013). By selecting an appropriate estimation method, L1 or L2 norm, for each of the three penalty terms, an actual inversion process can account for the statistical characteristics of the monitored data, the subsurface resistivity distribution and its temporal changes during the

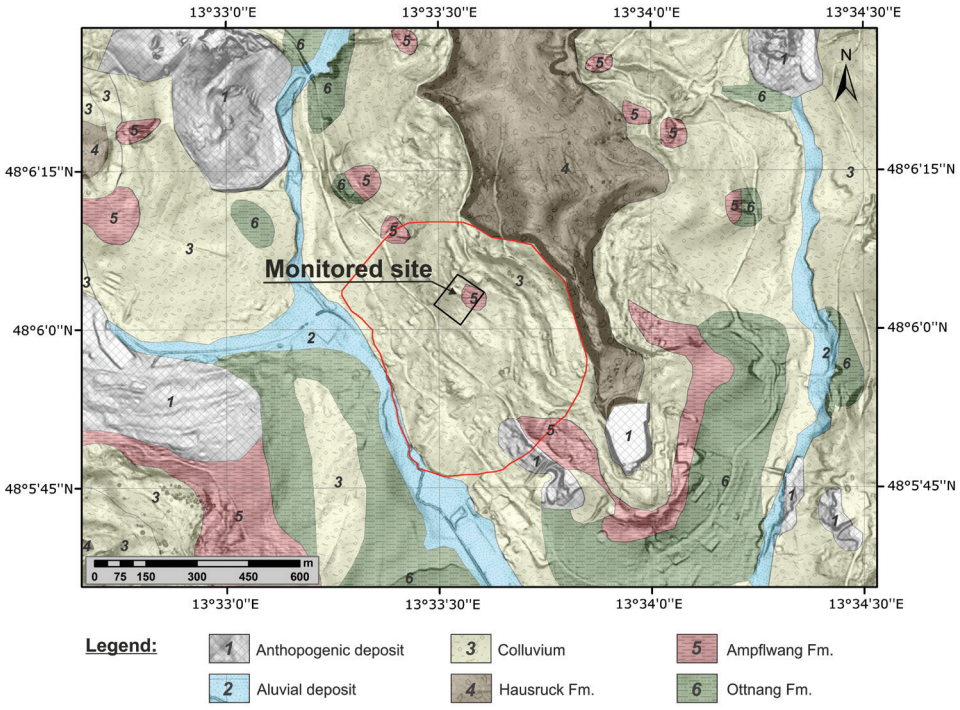

FIGURE 2
Map of the geological setting of the site according to the geological map ÖK47 (Ried im Innkreis, 1:50,000; GBA Wien 2008) showing the Ampflwang monitoring site. The red line delimits the area of the old deep-seated landslide; the black rectangle marks the monitoring site at the reactivated part of the landslide.

monitoring period. Particularly, we can easily cure a drawback of the original 4D inversion that adopts full L2 norm minimizations and sometimes results in a 4D model too smoothly varying with time (Karaoulis, Kim and Tsourlos 2011a; Loke, Dahlin and Rucker 2013).

A specific aspect of the algorithm used in this study is the automatic determination of two classes of the regularization parameters (Kim *et al*. 2012, 2013). The 4D inversion includes two smoothness constraints in the space and time domains, and correspondingly two different kinds of regularization parameters need to be optimally chosen. However, it is practically very difficult, since two different constraints in both the space and time domains would be cross-related in an actual inversion process. In our inversion code, two classes of the regularization parameters are automatically calculated based on the relative value of each penalty measure with respect to the data misfit penalty value. Accordingly, the parameter values are actively determined as the data misfits and model roughnesses vary and are updated at each iteration step.

Input data to the inversion code are the multiple time-lapse data sets, monitored during the period of interest. The output is a 4D resistivity model, which is spanned over the time period. From the inverted 4D model, the difference images with respect to a particular time instance are computed, and the ground condition changes are studied. For landslide studies we need to analyse the differences not only with respect to a particular reference time, but also between arbitrary pairs of time lapses. In this case, reasonable difference images can also be obtained from the inverted 4D model with little inversion artefacts. This greatly owes to the basic concept of the 4D inversion approaches that the entire monitoring data sets are simultaneously inverted. Thus, there is no dependence on the background data set as well as on the subsurface model obtained at a particular time.

THE AMPFLWANG-HAUSRUCK MONITORING SITE (AUSTRIA)

General characterization of the test site

The Ampflwang monitoring site represents a recent landslide reactivated after a house construction. It is situated in the surrounding of Ampflwang town in the Hausruck Hills in Upper Austria. The entire area north of the town of Ampflwang was affected by a deep-seated landslide in the Holocene. This dormant landslide is about 650 m long and 900 m wide, with an estimated depth of failure about 20–30 m b.g.l. It developed mostly in Quaternary colluvium (slope and old landslide deposits), anthropogenic deposits, and in the underlying Neogene rocks, i.e. fluvial gravels of Hausruck formation (4) at the top, limnic to fluvial coal-rich clay with brown coal beds of Ampflwang formation (5) in the middle, and in marine silty-sandy marl to silty sand of Ottnang formation (6) at the base (Fig. 2).

In March 2010, following snow melting and heavy rainfall, a shallow landslide was triggered in the vicinity of a newly constructed house in the central part of the old landslide (Fig. 2). It significantly damaged the surroundings of the house, i.e. parking lot, terrace, water and power supply, waste pipe, and put the house at risk due to retrogressive reactivations (Fig. 3). The reactivated part, as recognized by topographic changes and inclinometric data, is about 110 m long, 40 m wide and about 4 m thick and can be classified as a shallow rotational-translational landslide of elliptical shape.

Description of the local lithology based on the interpretation of geophysical data

Soon after the first displacement event two core drillings were performed. In both drillholes, geophysical borehole logging was performed, since this method can provide essential information on the local subsurface structure and for the lithological interpretation of the subsurface resistivity models. From the geophysical logging results and the core samples of the drilling at D.M.S. 1 (Fig. 4), a clear lithological structure could be derived: down to 1.8 m, gravels with resistivities of 50–70 Ω·m are dominating (anthropogenic deposits or Hausruck formation). The subjacent sandy layer is followed by clay (2.8–3.8 m) of the Ampflwang formation. Between 4 and 4.8 m a coal layer with low gamma count rates was detected, which is succeeded by silty sands (until 6.6 m) and marls (below) most probably of the Ottnang formation. A comparison with the inclinometric results clearly shows that the main sliding plane is located within the shallow clay layer.

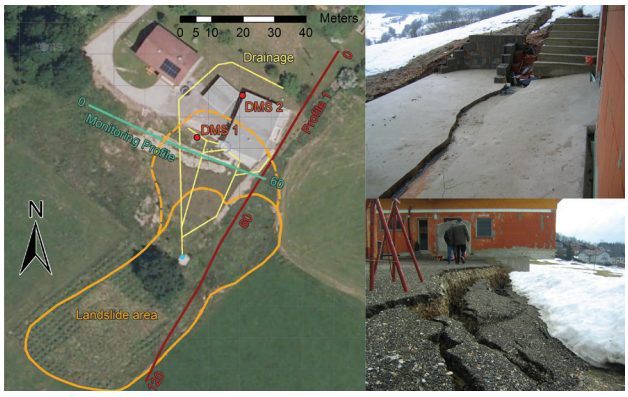

FIGURE 3
Location map (left) and documentation of damages (right up and down) at the newly constructed house at the Ampflwang/Hausruck test site caused by the shallow landslide in March 2010. (Photo: J. Gaisbauer)

A representative geoelectrical inversion model along the monitoring profile is shown in Fig. 5. Based on the borehole logging results described above, the high resistive surface layer can be interpreted as gravel, the areas with intermediate resistivity (green colour range, 50–100 Ω·m) as sand or coal and the low resistive (below 45 Ω·m) regions as silty clays. To investigate the general structure of the surrounding area of the reactivated landslide, additional geoelectrical measurements were performed along a profile perpendicular to the monitoring profile (for location see Fig. 3, for results Fig. 6). The profile comprised 125 electrodes at a spacing of 1 m, reaching a larger penetration depth of about 20 m. At the surface, a high resistive layer (150–

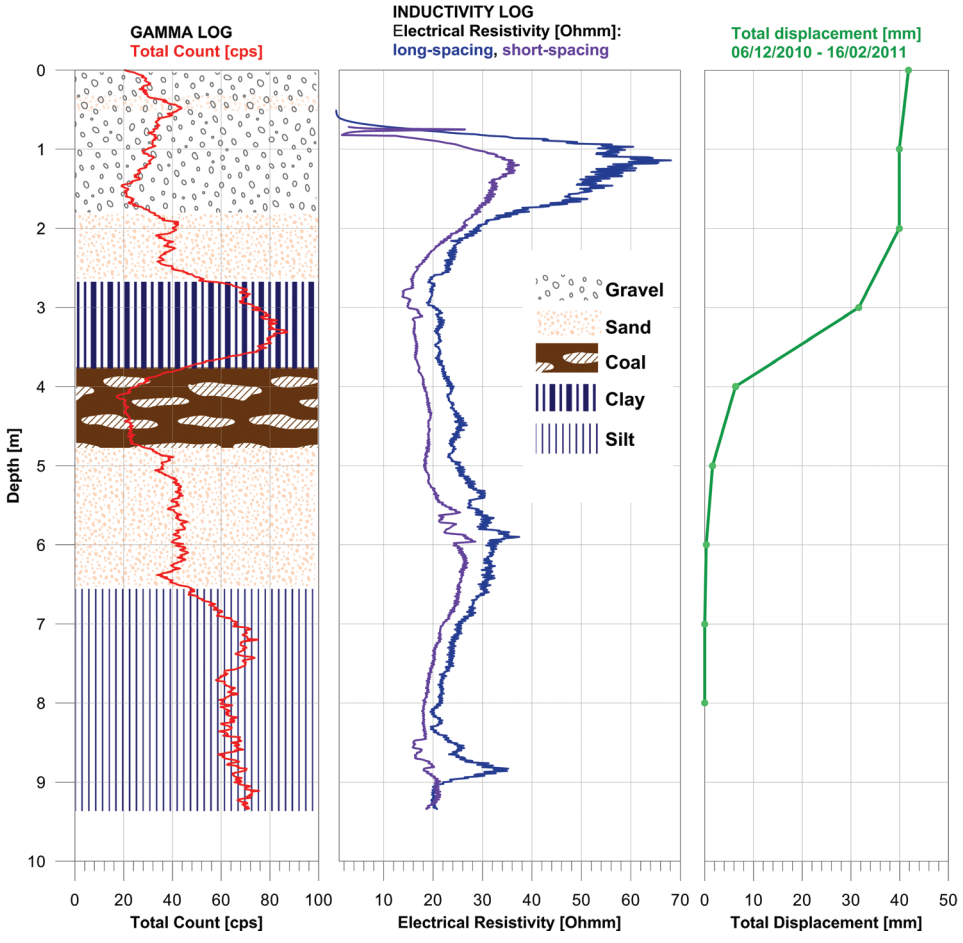

FIGURE 4
Results of borehole logging data at D.M.S.1: Gamma log (left), inductivity log (middle) and total displacement (right).

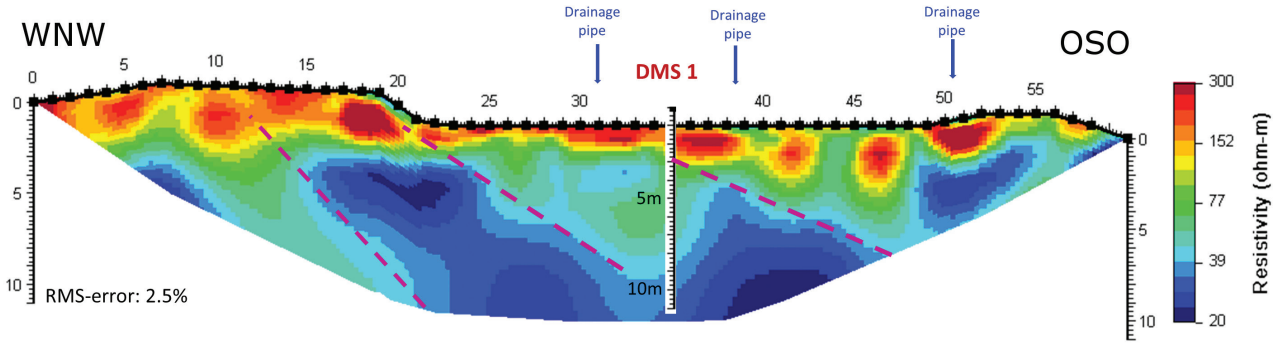

FIGURE 5
Geoelectrical inversion results of measurements from the monitoring profile.

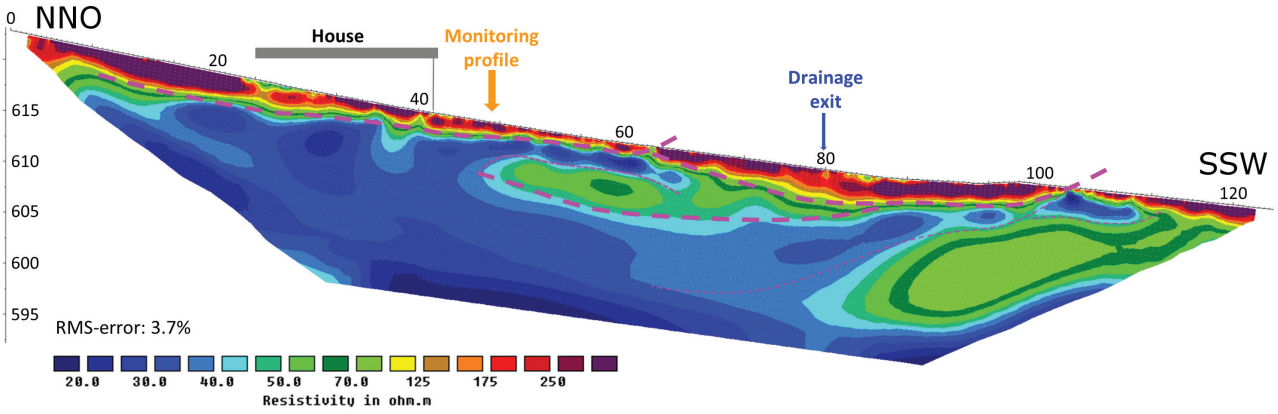

FIGURE 6
Results of geoelectrical inversion along profile 1.

500 Ω·m) with variable thickness (0–7.5 m, again interpreted as gravel of the Hausruck formation or of anthropogenic origin) can be found, followed by at least 15 m of low resistive clays. In the middle and at the end of the profile, intermediate layers with a resistivity between 45 and 70, and 60 and 100 Ω·m, respectively, could be determined. The first one has been interpreted as silty sand of the Ampflwang formation, most likely identical to the lower sand layer of the D.M.S. 1 hole, the latter one most probably as sand of the Ottnang formation. The structure of the derived subsurface model gives indications of possible past sliding events (possible sliding planes are indicated by purple lines in Fig. 6).

Design of the monitoring network

Due to the high potential hazard (directly endangered family house) and to develop an optimized strategy for site-specific remediation measures, a permanent, fully automated monitoring system, consisting of two D.M.S. columns and a geoelectrical monitoring device, was set up in December 2010. Precipitation data for the interpretation of the monitoring results were taken from the weather station of Wolfsegg (8 km distance to the monitoring site), courtesy of the Central Institute for Meteorology and Geodynamics (ZAMG). One of the D.M.S. columns (D.M.S. 2) was installed upslope of the house, the other one (D.M.S. 1) was positioned close to the expected crown of the landslide downslope of the building. The D.M.S. columns included high resolution tilt/displacement, temperature and piezometric sensor modules and registered displacement data on an hourly basis down to depths of 5 and 7 m b.g.l., respectively.

The geoelectrical GEOMON^{4D} monitoring profile, which comprised 61 electrodes at a spacing of one metre, was installed inside a shallow drainage trench downslope of the house and close to D.M.S. column 1 (Fig. 3). One set of data, comprising around 1800 gradient-type measurements, was taken every 4 hours. For power supply a connection to the local power grid was installed.

Analysis of displacement monitoring data

Measurable displacements were only registered in D.M.S. 1, situated below the building in the upper part of the landslide (Fig. 3). The inclinometric record of cumulative displacement along the N-S plane (Fig. 4) showed a quite sharp slip surface between a depth of 2.5 and 3.5 m b.g.l., with a general direction of movement towards the SSW. When compared with the geoelectrical results, we can correlate the top of the first low resistive layer (2.8 m) as the approximate location of the sliding plane. However, due to the limited length of the inclinometer, it could not be deter-

mined whether another active sliding plane exists at the top of the second low resistive layer at around 8.5 m depth. Possible sliding planes were indicated as purple dashed lines in Fig. 5.

Major displacement events within the monitoring period (Fig. 7) occurred after snow melt and during intense rainfall between January and March, except event 2, which was most probably triggered by snow melt and/or ground thaw only. After the middle of July the velocity decreased to almost zero, although quite frequent and intense rainfalls took place. At the end of August 2011, the monitoring device had to be removed due to remediation measures at the location of the system.

Analysis of resistivity monitoring data

Figure 8 shows a summary of the results of all performed measurements for the entire survey period. This general plot is used to check the performance of the system and to detect general tendencies and dependencies on precipitation (plotted at the left-hand side of Fig. 8). It represents normalized, dimensionless

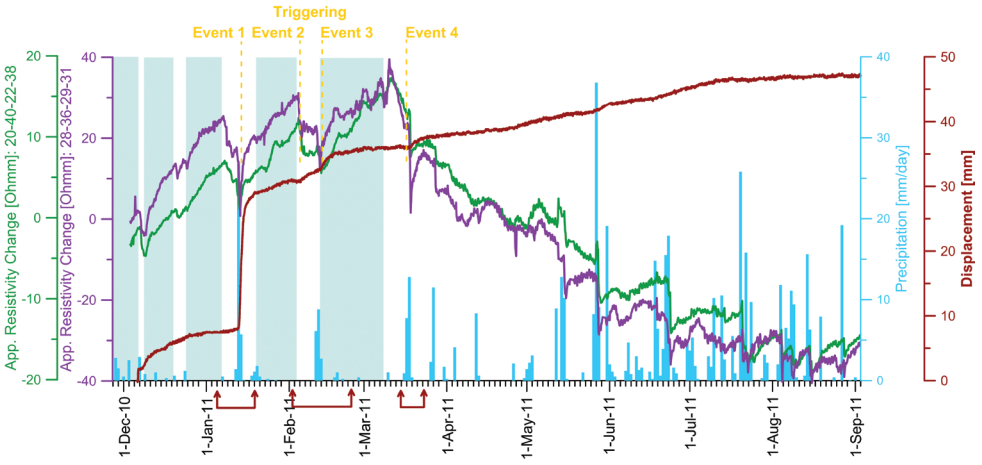

FIGURE 7
Graph of cumulative displacement (dark red) compared to total daily precipitation (light blue, courtesy of the Central Institute for Meteorology and Geodynamics (ZAMG)) and apparent resistivity at different relative apparent depths (green: 3.5 m; purple: 1.5 m) for the whole survey period; areas with ice blue shading: times with air temperatures below 0°C, profile location 30–32 m. The three red arrows mark the sections which are zoomed in Figs 10–12.

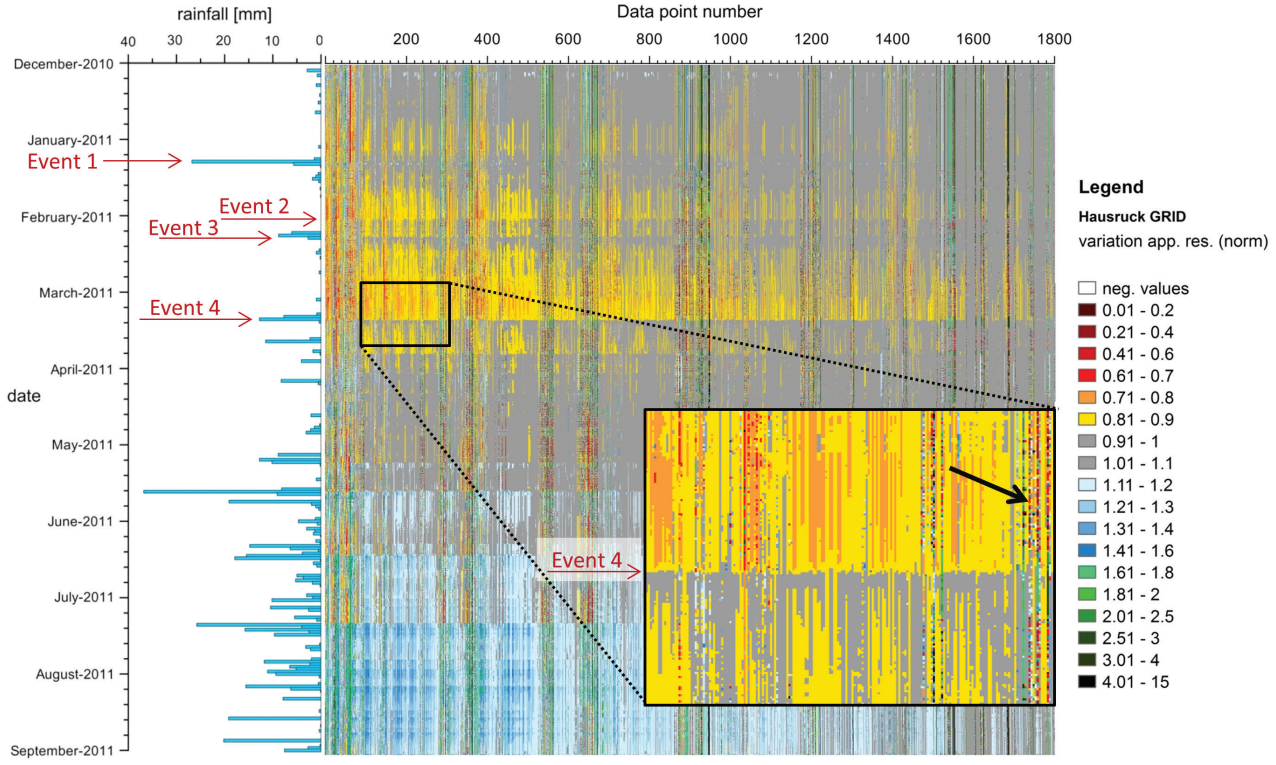

FIGURE 8
Normalized values, which were calculated by using equation (1), reflecting resistivity changes from all performed measurements for the whole survey period.

values, corresponding to a change of apparent resistivity, plotted in a grid. It includes data points of all measured electrode configurations (increasing pseudo-depth of the configuration with increasing data point number) for the entire monitoring period. The normalization is performed for each data point separately with the following equation:

$$normalized\ value(N) = \frac{\sum_{i=0}^{N-1} app.res_i}{N-1} / app.res_N \qquad (1)$$

Values which are smaller than 1 represent an increase of apparent resistivity compared to the average apparent resistivity of all previous measurements (e.g., a value of 0.5 is equivalent to a doubling of apparent resistivity), whereas values larger than 1 stand for a corresponding decrease.

This plot is analysed on a daily basis since the general data quality can be easily assessed: general malfunction of the system can be detected with one view as well as electrode configurations affected by a large noise component (lines deviating from the general trend and with strong, short-term variations – within the zoomed section of Fig. 8 indicated by the black arrow). The latter configurations are removed for the inversion process.

Moreover, this plot clearly reflects the influence of precipitation on the majority of measured configurations. Precipitation events are accompanied by a significant decrease of apparent resistivity. The zoomed section in Fig. 8 shows the decrease correlated with the triggering event 4, where the normalized values changed from yellow (0.81–0.9) to grey (0.91–1.1). The general difference of normalized values between winter (orange to grey dominate) and summer (grey to blue dominate) is related to the seasonal change of soil temperature.

Analysis of the time dependency between resistivity decrease and landslide triggering

To analyse the time dependencies in detail, two representative time series of apparent resistivity values were selected from configurations corresponding to different apparent depths in the middle of the profile. The results are displayed in Fig. 7 in correlation with precipitation and total displacement over the whole monitoring period. This figure confirms that most of the major rain events were accompanied by a resistivity decrease.

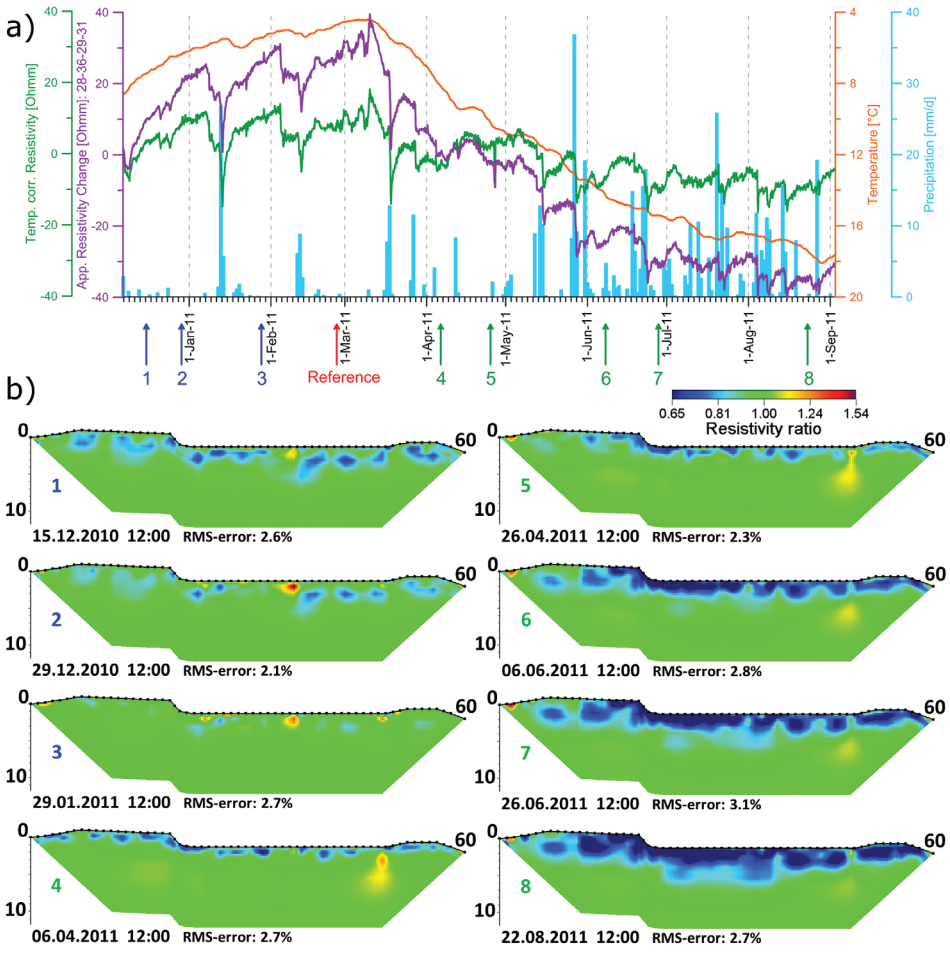

FIGURE 9

a) Apparent resistivity at relative apparent depth of 1.5 m and apparent resistivity corrected for the temperature effect, compared to precipitation and temperature. The temperature dependence of resistivity is calculated by $\rho(T2) = \rho(T1)*((T1 + 21.5) / (T2 + 21.5))$ and then subtracted from the measured resistivity (green line). b) Resistivity changes of 4D inversion result for the whole survey period, calculated to a reference measurement on 27 February (t_0). The inversion results show the influence of temperature on subsurface resistivities; the resistivity ratio is calculated by $\rho(t)/\rho(t_0)$.

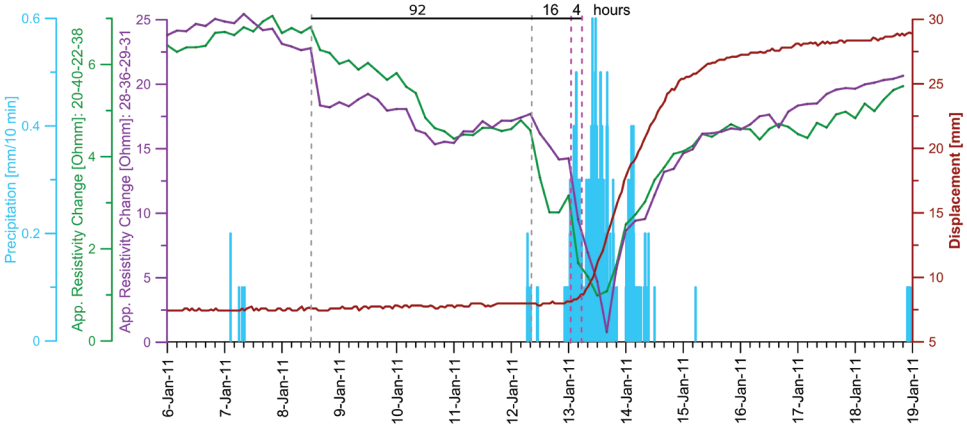

FIGURE 10
Display of displacement (red), precipitation (blue; courtesy of the Central Institute for Meteorology and Geodynamics (ZAMG)) and apparent resistivity at different relative apparent depths (green: 3.5 m; purple: 1.5 m) for the time around the major displacement event (event 1) in January 2011.

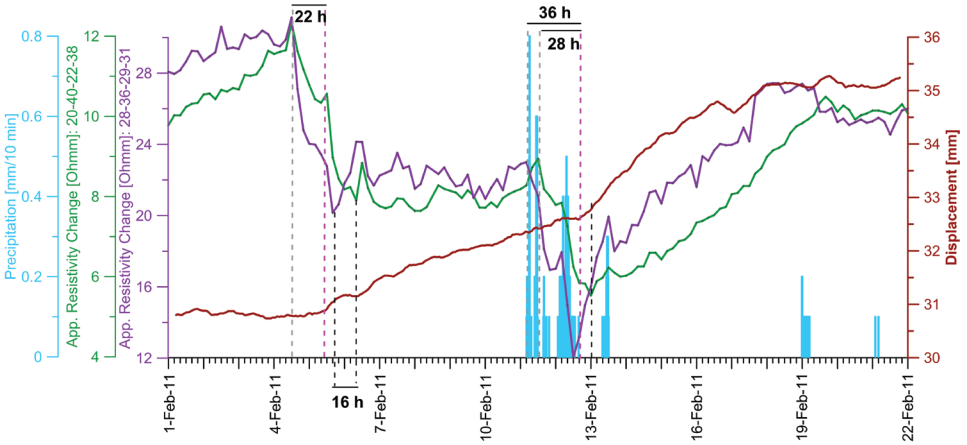

FIGURE 11
Display of displacement (red), precipitation (blue; courtesy of the Central Institute for Meteorology and Geodynamics (ZAMG)) and apparent resistivity at different relative apparent depths (green: 3.5 m; purple: 1.5 m) for the time around events 2 and 3 in February 2011.

The total monitoring period can be subdivided into two phases: the first one (December until the beginning of March) with alternating phases of freezing and thawing is characterized by a general increase in resistivity. All major displacement events took place in this period and are correlated with a short-term decrease of resistivity. Typical for this period is that the decrease of resistivity started some time before the onset of rain, most probably due to pre-wetting of the subsurface caused by snow melt and/or ground thaw.

The second phase (March until September) shows a general decrease in resistivity. Almost all major rain events are correlated with an abrupt resistivity decrease, in many cases preceded by a short-term resistivity increase.

A comparison with soil temperature (Fig. 9) shows that the long periodic trend is mostly caused by variations of soil temperature. After correction for the temperature effect (green line in Fig. 9), hardly any long periodic trend is left. A 4D inversion of the data (lower part of Fig. 9) also proved that the long-term variations of resistivity are constricted to the first 4 m. Below, temperature changes can be neglected (Fig. 9). However, when analysing the whole data set on temperature dependency, it turned out that corrections for temperature are very dependent on the respective location. Since temperature monitoring was available only at one location and because we focus mainly on the short-term events in the following discussion, such corrections were generally not applied.

Figure 10 focuses in detail on the period around 'Event 1-E1'. Resistivity values already started to decrease around 8 January, most probably due to an inflow of water from snow melting. This trend continued until a first short rainfall on 12 January, after which the resistivity decrease accelerated. Following the onset of an intense rainfall before midnight on 12/13 January, apparent resistivity further decreased until around 07.00 when the main movement was triggered. The acceleration phase of the landslide lasted until 13.00. After 16.00 resistivity started to increase rapidly and displacement decelerated, although precipitation continued with less intensity for almost one day. The total displacement reached 18.5 mm in 58 hours.

Except for three other small events (E2-5) of increased acceleration, the landslide showed only a small and quite constant displacement for the rest of the observation period. Data from E2 and E3 in February (Fig. 11) and E4 (Fig. 12) in March show a quite similar behaviour.

The periods of resistivity decrease (phase of 'pre-wetting') before the onset of the rainfalls amounted to 4.5 (E1), 6.5 (E2-E3) and 9 (E4) days. The delay times between the start of the final abrupt resistivity decrease at 1.5 m depth and the triggering of the landslide were determined as 16 (E1), 22 (E2), 36 (E3) and 16

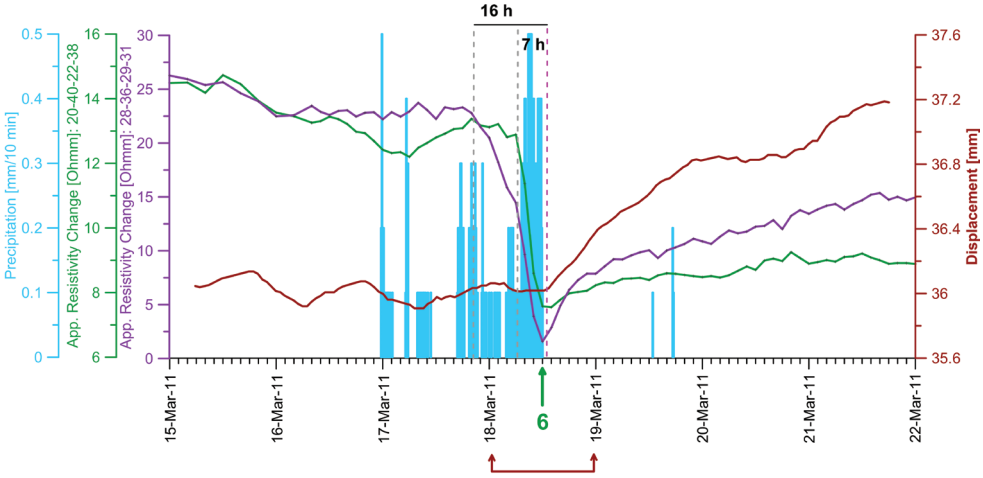

FIGURE 12
Display of displacement (red), precipitation (blue; courtesy of the Central Institute for Meteorology and Geodynamics (ZAMG)) and apparent resistivity at different relative apparent depths (green: 3.5 m; purple: 1.5 m) for the time around event 4 in March 2011. The red arrow marks the period related to the 4 D inversion in Fig. 14, whereas the green arrow marks time step 6.

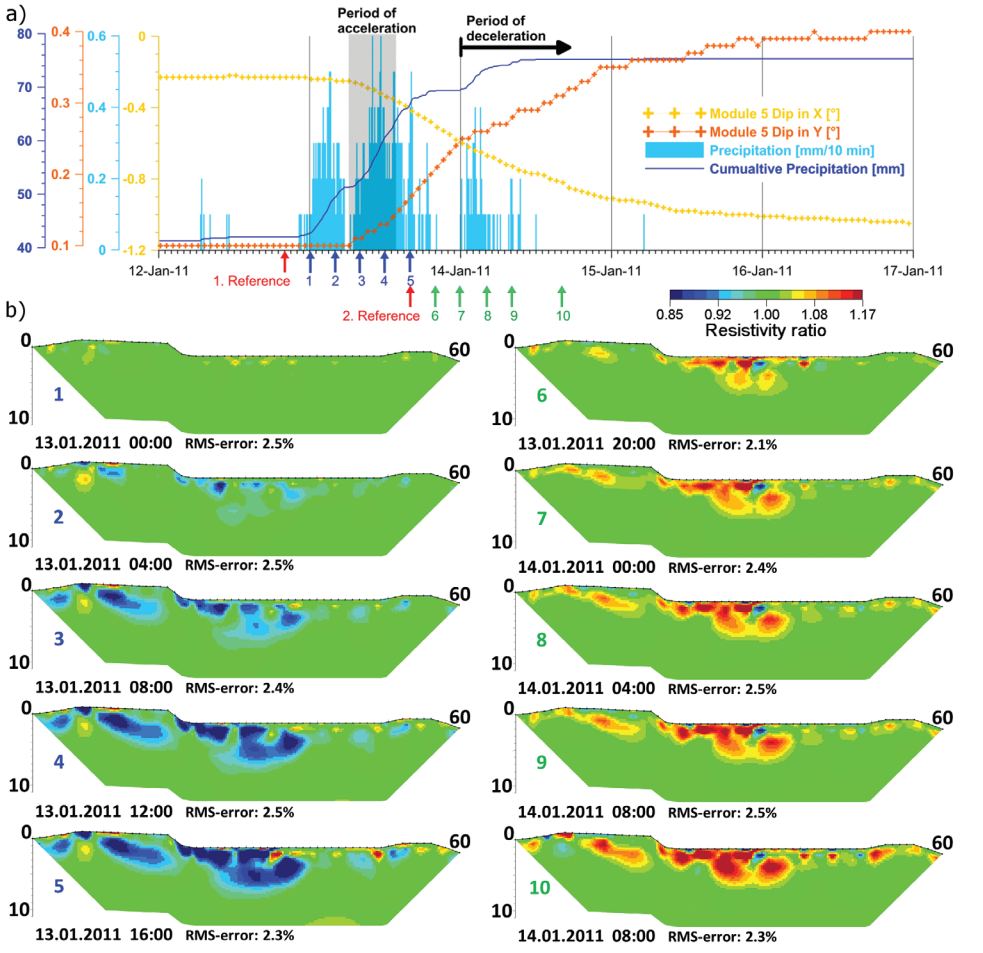

FIGURE 13
a) Precipitation, cumulative precipitation and dip angle of inclinometer module 5 for the period when event 1 took place. b) Resistivity changes of 4D inversion result for the period between 12 and 17 January (event1), calculated to a reference measurement on 12 January at 20.00 (left column) and to a reference measurement on 13 January at 16.00 (right column). The resistivity ratio is calculated by $\rho(t) / \rho(t_0)$.

(E4) hours. For larger electrode spacings and greater depths, a time delay of 7 to 8 hours (E4-5) can be observed (green curve).

Analysis of the time dependency between resistivity decrease and depth

Figure 13 shows the 4D inversion results of resistivity data measured between the 12 and 15 of January ('event 1'). Differences refer to two different reference measurements (indicated by red arrows in Fig. 13) for the period before and after triggering of the landslide. Rainfall started around 22.00 on the 12th. The acceleration of the landslide was initiated around 07.00 on the 13th and lasted only until 14.00, when a phase of almost constant speed developed, lasting until midnight. After that, although rainfall continued, the landslide slowed down again. This behaviour is

clearly reflected in the resistivity inversion results. Until 04.00 in the morning of 13 January only minor resistivity changes were detected, restricted to the surface layer (times 1 and 2 in Fig. 13). At the time of the triggering of the landslide, the inversion data proved that the wetting front had already penetrated down to the second sandy layer (time 3 in Fig. 13). Afterwards resistivity further decreased until the end of the acceleration phase (times 3–5 in Fig. 13). Although precipitation continued, the subsequent inversion results (time steps 6–10 in Fig. 13) show an increase in resistivity. To enhance the effect of resistivity increase in the 4D inversion results, a different reference was used for time steps 6–10.

Data from the other events gave similar results. As an example, Fig. 14 shows the 4D inversion results for event 4. Again, the movement was triggered when the resistivity decrease reached the lower sand layer (time 6, for movement triggering see Fig. 12), and lasted only until the end of the acceleration phase. However, the resistivity increase afterwards was not as rapid as after event 1.

Discussion of results from the test site Ampflwang

We can summarize that for all detected sliding events, we could observe a decrease in the apparent resistivity before and during the acceleration phase of this landslide, starting several days before the onset of the precipitation, which finally seemed to have triggered the displacement events. The inversion results clearly showed that the reduction of resistivity values before the triggering event was limited to the surface layers. The delay between the first onset of resistivity decrease (most probably induced by snow meltwater) and the triggering of the landslide was 4.5 to 9 days. A delay between resistivity decrease detected on the small (shallower) and the large (deeper) electrode separations of more than 8 hours was detected for some events, being a measure of the speed of penetration of the wetting front into the subsurface. Immediately after the acceleration had stopped and a phase of constant movement was reached, resistivity values started to increase again. The inversion results definitely suggest that the landslide was only triggered when the wetting front reached a certain depth (i.e. the second sandy layer, for reference see Fig. 4).

Since no acceleration event was monitored in late spring and during summer, when even more intense rainfalls took place, causing a resistivity decrease of almost the same amount but of different shape, the results imply that pre-wetting of the subsurface by snow meltwater is a premise for the triggering of this landslide. However, we also cannot exclude that the landslide in general had stabilized during the summer period. Further facts to understand this landslide could have only been derived if the monitoring had been continued for another year. Unfortunately, this was not possible due to scheduled remediation measures.

THE BAGNASCHINO MONITORING SITE (ITALY)

General characterization of the test site

The Bagnaschino site (Fig. 15), located about 4 km SE of Torre Mondovì in the Casotto valley in the province of Cuneo/Piedmont, represents a complex landslide reactivated within an old, deep-seated gravitational slope deformation (DSGSD) mass. This DSGSD is most probably structurally controlled. Its base and upper trench most likely follow the active regional thrust fault.

The unit of Bagnaschino, eradicated from the Brianzonese domain (part of the crystalline basement) was thrusted over the Villanova formation, belonging to the Piedmont domain. Following this event, a series of brittle tectonic elements was superimposed over the two formations. The geological structure of the area was studied by several core boreholes (Peisino *et al.* 2009b). The main rocks, recognized underneath the colluvial clastic deposit, are intensely fractured mica schists and amphibolites (Bagnaschino formation). These rocks reached a high level of metamorphism (green schist). The Villanova formation lying

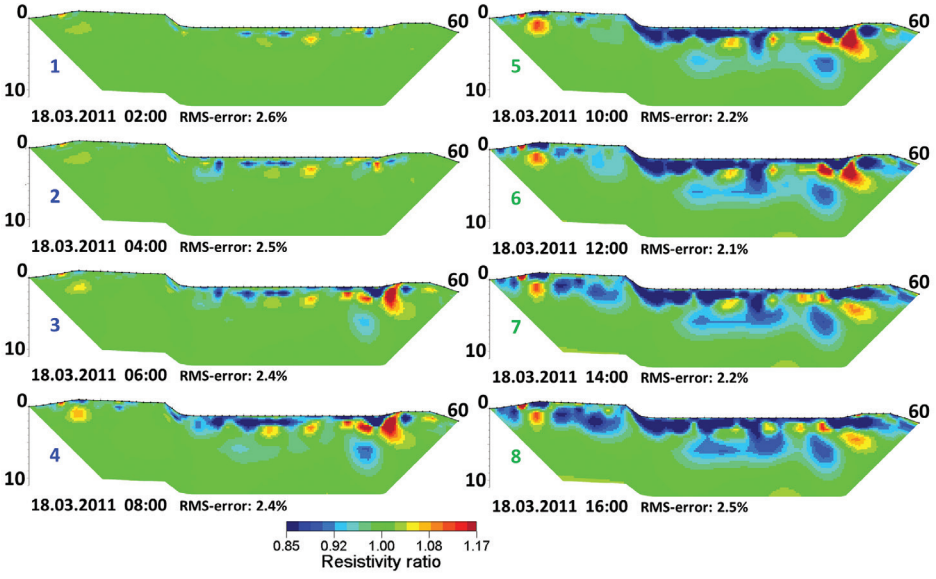

FIGURE 14
Differential 4D inversion results for event 4: resistivity changes are calculated to a reference measurement on 18 March at 00.00. The resistivity ratio is calculated by $\rho(t) / \rho(t_0)$.

below is composed of limestone and dolomites, characterized by diffuse karstification (Giuliani *et al*. 2010).

The entire Bagnaschino landslide was recognized and mapped in the frame of the Inventario dei Fenomeni Franosi in Italia (IFFI) project in 1979. Debris and small boulder falls consistently affected the road called SP n. 164. However, the main recent event, related to the active landslide, occurred in November 1994 after a distinct heavy rainfall event. It caused an interruption of the SP n. 164 road and also partly dammed the Casotto creek. After another reactivation in October 1996 a protective tunnel was realized to safeguard the road.

The active landslide covers an estimated area of 150 000 m^2 and comprises 1.2 million m^3 of displaced material (only the flow part). It is a rotational-translational landslide of an elliptical shape and with a depth of failure at about 8 m b.g.l. A sketch of the geological cross section (based on Peisino *et al*. 2009a-c) along the monitoring profile is shown in Fig. 16. Based on the data so far available (Lovisolo 2011), it can be concluded that the displacement developed in distinct relation to rainfall events or snow melting.

Design of the monitoring network

To continuously monitor the stability conditions of the landslide, the Province of Cuneo (Civil Protection Office) established a slope monitoring plan in 2008. A 60 m long D.M.S. column was installed in October 2008 (Peisino *et al*. 2009c) and registered five critical events between autumn 2008 and spring 2009, which reactivated the landslide along a sliding surface at 7 m b.g.l. All events were clearly triggered by snow melting and/or heavy rainfall (Lovisolo 2011). In July 2009, when a maximum displacement of 60 cm was reached, this column was removed, since its operation could not be guaranteed for larger displacements. As a consequence, the column was repaired and separated into two parts. The upper column, 20 m in length, was installed in a separate hole to monitor the shallow and fast displacements (D.M.S. 1). For the lower column, 40 m in length (D.M.S. 2), a hole with a diameter of 1 m was excavated down to a depth of 20 m to allow for larger movements in the shallow part without destruction of the deeper system. Below the 20 m of the hole, drilling was performed with the usual inclinometric diameter on the downhill side of the bottom of the 1 m hole, thus allowing a high resolution monitoring of the deeper, much smaller displacements. For the purpose of interpretation, it has to be kept in mind that the colluvial mass, which was excavated for the installation of the deep D.M.S. system and then deposited again, could have undergone some degree of settlement since then. This settlement could influence the local observations at shallow depth, although the new drillhole for the shallow D.M.S. was performed several metres away. The dual D.M.S. system started its operation in June 2010.

Subsequently, in October 2010 a geoelectrical monitoring system was added using the GEOMON^{4D} technique. One profile was installed along a W-E line from the top to the bottom of the landslide (Figs 15 and 16) and consisted of 93 electrodes. In the upper part, starting almost at drillhole S4, until 40 m after the midpoint of the array, which was positioned close to the D.M.S. systems, the monitoring cables were buried in a trench. However, in the lower part of the profile down to the protection tunnel, the cables had to be fixed at the surface due to slope steepness. An

FIGURE 15
Location of the Bagnaschino monitoring site (Photo by R. Supper, small picture modified after bing-aerial maps). The area of the landslide is indicated by the orange dashed line; the red line marks the location of the monitoring profile.

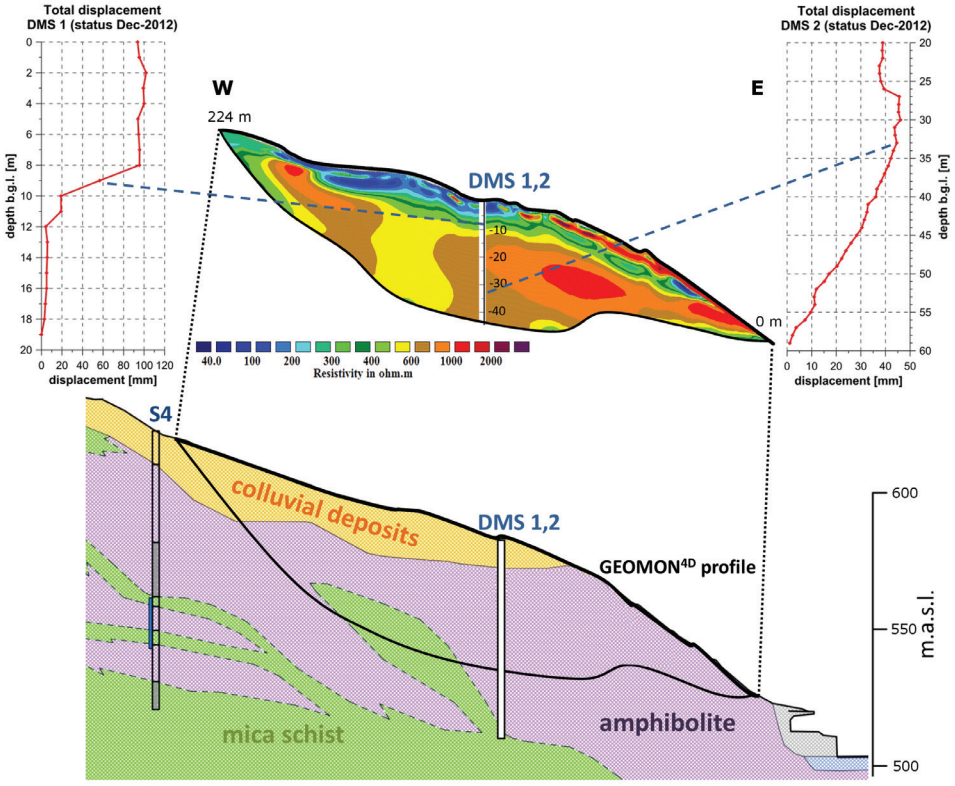

FIGURE 16
Correlation of resistivity layers with a sketch of a geological cross section and results of inclinometric monitoring.

alternative layout of electrode configuration with variable electrode distances was used to achieve both a high resolution around the D.M.S. station as well as to gather information about resistivity variations at larger depths (maximum 40 m). Therefore the electrode separation along the profile was varied from 1 m in the middle of the profile to 2 m, 4 m and finally 8 m for the outer electrodes. A solar panel – fuel cell combination was used as the power supply of the geoelectric system. Every day, two data sets of high-resolution data from just the inner electrodes with a spacing of 1 m, and two data sets involving all electrodes, were measured. During the time of the March event, the measurement interval was increased to six measurements per day and self-potential was measured hourly.

Precipitation data were available from the weather stations Viola and Pamparato (6–7 km distance), operated by the Province of Cuneo. Piezometric data were available from the deep D.M.S. column (although the casing is not perforated) and one automatic station inside drillhole S4 near the end of the geoelectrical profile (perforation at a depth of 63–72 m).

Interpretation of the resistivity inversion model along the monitoring profile

Figure 16 shows the correlation of a representative resistivity inversion result along the monitoring profile with the dynamic evolution of the landslide. Layers with diverse displacement patterns are well delineated by bodies with different electrical properties. The shallow surface layer (thickness of approximately 9 m), which exhibits the highest displacement rate, shows a relatively low electrical resistivity below 450 Ω·m (colluvial and detrital deposits). Based on the resistivity inversion and core mapping results we can subdivide this layer into a surface layer with a high clay content (75–250 Ω·m, down to 6 m) and a more compact colluvium layer with higher content of rock fragments and less clay and porewater (250–450 Ω·m, 6–9 m at the D.M.S. location). The inclinometric results suggest that during the first D.M.S. observation period, movements rather took place at the border between the different colluviums layer (6–7 m, i.e. the more clayey layer sliding on the more compact stratum), whereas during the second observation period, a slipping plane at the base of the colluvium (8–10 m) was activated. The latter slides on a highly resistive, partly fractured and weathered amphibolite body (500–1500 Ω·m), which exhibits an almost constant (with depth) creeping behaviour with low movement rates. Below 35 m of depth, a layer with lower resistivity (below 600 Ω·m) emerges, which might correlate with schist or more fractured amphibolite. The lower resistivity anomaly at medium depth in the middle of the profile (400–600 Ω·m) most probably correlates with a schist layer also mapped inside several drillholes (see geological sketch in Fig. 16). Along the eastern part of the slope, talus material and/or heavily fractured and moved host rock is found as the surface layer (> 1000 Ω·m). The high resistivity is caused by a large amount of air-filled fractures, which might be partly filled up by water in the case of increased groundwater flow (rela-

tively high hydraulic conductivity). Below, a medium resistive layer (250–450 Ω·m, lower hydraulic conductivity compared to the surface cover) can be interpreted as heavily weathered host rock, perhaps in its original position, followed by more compact amphibolites (600–1500 Ω·m), which outcrop at the base of the profile.

Analysis of displacement data during the geoelectrical monitoring period

After the installation of the dual D.M.S. system the temporal evolution of displacement (observation period 19 October 2010 – 18 September 2012) exhibited a quite stable behaviour. Only one large (9.5 cm, March 2011) and one small (around 1 cm, March 2012) short-term reactivation event (Fig. 17) could be detected.

The inclinometric results (Fig. 16) identified a slipping zone between 8–10 m b.g.l., which can be correlated with the base of the colluvium deposit. At larger depths (20–60 m b.g.l., Fig. 16), a slow and continuous creeping of about 3.5 cm can be detected, which shows constant acceleration rates with depth below 35 m. Above, the high resistive block between 10 and 35 m seems to move with constant speed; no differential movements were detected.

The main displacement event within the second D.M.S. monitoring period happened in March 2011. This event (Fig. 18) is characterized by an acceleration phase lasting for almost 7 hours, correlating with the period of the highest precipitation rates. For the following 7 hours the velocity of the landslide was almost constant (maximum velocity ~3.5 mm/day), followed by a period of smooth deceleration (although the rainfall still continued). The total displacement reached about 70 mm in 64 hours. The only other distinct event happened in March 2012 with a total displacement of 10 mm.

Analysis of groundwater level data

Water levels were continuously recorded inside the deep D.M.S. pipe (which is in general unperforated and therefore the water level is filled up by inflow of water originating within the colluviums layer) and inside drillhole S4 (for location see Fig. 16, water level in Fig. 17), located at the upper end of the geoelectrical profile close to the supposed scarp of the landslide.

Drillhole S4 encountered a confined aquifer at a depth of 63–72 m b.g.l. In the observation period before the March event, successive major rainfall events (above 20 mm/day) caused the water table in S4 to rise from –16 to –9.4 m b.g.l. and from –59 to –55 m in the D.M.S. 2 hole (Fig. 17). This rising water table in S4 suggests that an inflow of artesian water from a deeper aquifer into the near surface colluvium layer might have taken place and could have preconditioned the triggering of the slide.

Before the triggering of the movements and during the main acceleration phase, the D.M.S. 2 water level did not show any significant changes, whereas the water level in S4 was smoothly rising. At both sites the major phase of water level rise was delayed and started only after the end of the main acceleration phase (16 March). The highest water level in D.M.S. 2 was reached on the 25 March (–42 m b.g.l.) and in S4 on the 30 March (–2 m b.g.l.). Afterwards, water levels in both holes started to drop. Inside the D.M.S. column no water level could be detected after 3 May (level below 60 m b.g.l.), whereas in S4 the water level dropped continuously until August (last data available). In that period, no influence on the water level due to further rainfalls could be observed, although heavy precipitation events definitely took place.

Analysis of resistivity monitoring data

Figure 18 shows difference images of the 4D inversion of the geoelectrical data in the central section of the profile for the

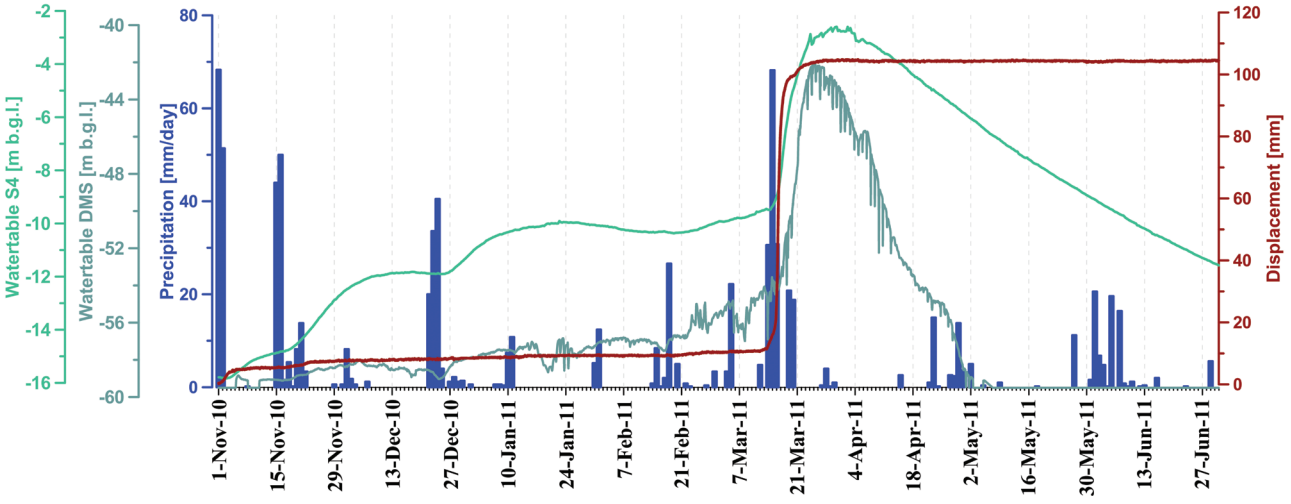

FIGURE 17

Graph of displacement (dark red), compared to total daily precipitation (dark blue), to groundwater level in DMS column (glaucous), and to water level at S4 (green).

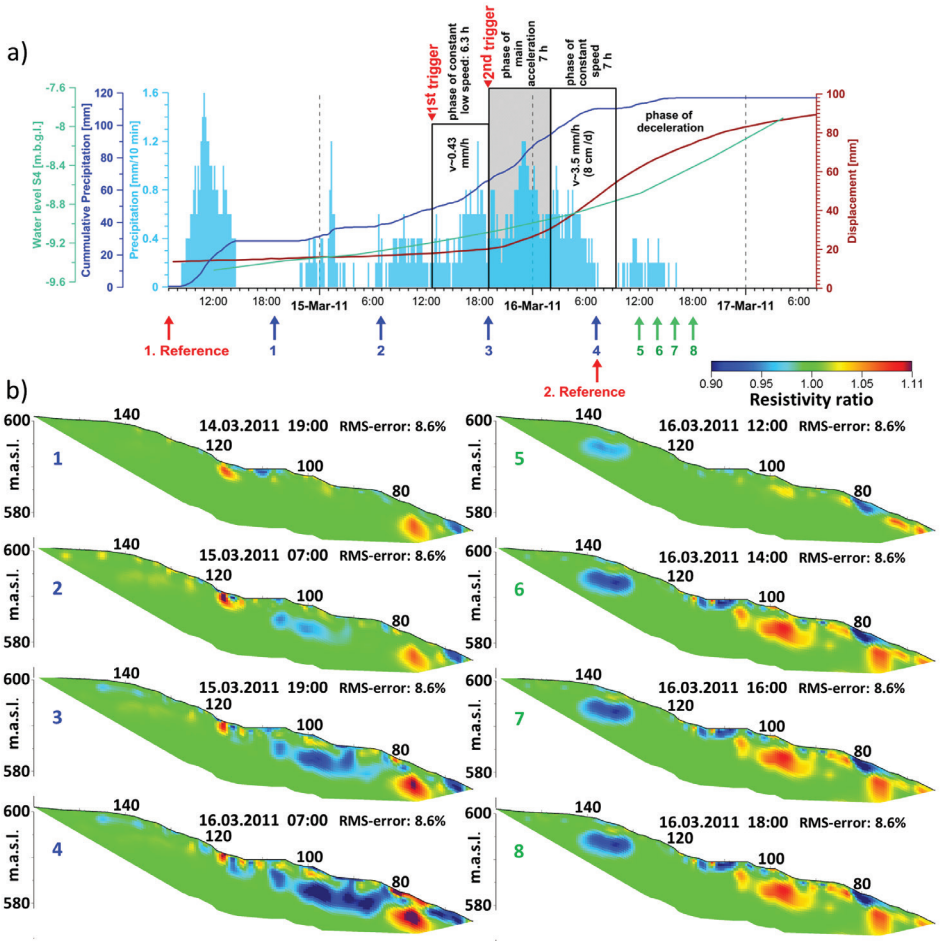

FIGURE 18
The 'March 2011 event': a) Graph of cumulative displacement (red), compared to total 10 minutes precipitation (light blue), cumulative precipitation (blue), and to water level registered at piezometer S4 (green) from 13 to 20 March 2011. b) Differential 4D inversion results for the March 2011 event: resistivity changes are calculated to a reference measurement on 14 March at 07.00 (left column) and to a reference measurement on 16 March at 07.00 (right column). The resistivity ratio is calculated by $\rho(t) / \rho(t_0)$.

event in March 2011, whereas Fig. 19 illustrates the results of the 4D differential inversion superimposed on to the geoelectrical inversion results. To highlight the trends in different phases of the event, differences in two diverse reference data sets (i.e., 14 March 07.00 for the acceleration phase and 16 March 07.00 for the deceleration phase) were calculated (Fig. 18).

On 14 March, a very small isolated resistivity anomaly developed after the first period of rainfall, most probably related to the direct inflow of surface rainwater (supported by an enhanced hydraulic conductivity in that area due to the excavation work related to the recovery of the old D.M.S. system). During the following night a significant resistivity decrease (step 2) took place in an area downhill of the D.M.S. system at a depth between 4 and 7 m, which enlarges successively and penetrates towards larger depth (step 3). On 15 March 2011 at 13.00 (Fig. 18) the major reactivation event (displacement of 7 cm in one day) was triggered. During the major landslide acceleration phase (between steps 3 and 4), resistivity further decreased by about 10% (saturation increases) and the anomaly further enlarges downhill (step 4), but only within the surface layer, i.e. the slope scree. After that period, resistivity increased again, except at one isolated region uphill of the D.M.S., where a new negative anomaly developed.

Discussion of results from the test site Bagnaschino

The results of the 4D inversion suggest that the area affected by the event was restricted to a region close to the D.M.S. system, where colluvial deposits verge on the almost outcropping, weathered amphibolite and slope scree (as a thin surface layer). Compared to the porosity of the colluvium, the amphibolites represent a relative aquiclude. The resulting basin-like structure was successively filled up with water due to inflow of water (rainfall, groundwater from the colluviums above). Part of the water overtopped the edge of the colluvium basin and entered the thin slope scree layer downhill, where resistivity also decreased significantly. Going hand in hand with an increase of the saturation, the shearing resistance of the colluviums was successively decreased, until a certain level was reached, when a movement was triggered along the base of the colluviums. We assume that due to the movements, fractures opened and groundwater dissipated into deeper structures. This could explain the fact that the water level in the deep D.M.S. hole starts to rise only after the acceleration phase. The subsequent decrease in saturation is indicated by the fact that subsurface resistivity starts to increase again (steps 5–8) in Fig. 18. During steps 5 to 7, another but isolated resistivity low developed uphill of the D.M.S. location. This anomaly appeared only after the end of the precipitation event, at

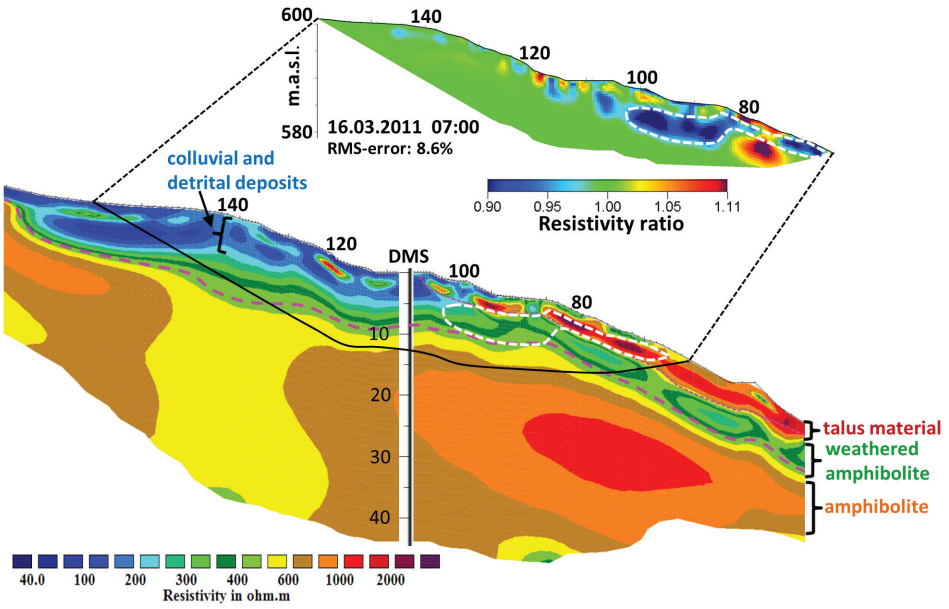

FIGURE 19
Illustration of the interpretation of the geoelectrical subsurface model (bottom, hatched white line indicates area of maximum resistivity decrease during the March 2011 event) and 4D inversion (top right) results of the March 2011 event. Purple lines indicate possible sliding planes derived from the geoelectrical results.

the same time as when the water level rise in S4 was initiated. Since two other abandoned drillholes were located close to this area, this resistivity decrease could also be caused by inflow of artesian groundwater from a deeper confined aquifer.

To sum up, at this site the results of the geoelectrical monitoring could contribute significantly to the understanding of the possible processes involved in the March event. From the results of the geoelectrical monitoring, it can be concluded that the affected area was rather small and no larger hazard could be expected.

The detection of displacements, their triggering events and determination of delay times of associated subsurface processes were possible using a combined monitoring of geoelectrical and geotechnical properties with a high sampling frequency. This multiparameter monitoring approach significantly improved security of the traffic on the road at the landslide's toe and the Civil Protection interventions. For example, based on the prompt monitoring results, the Province of Cuneo closed road no. 164 on 13 March and reopened it again on 21 March, when the displacement had stopped.

CONCLUSIONS

The analysis of data from two test sites proved that most recorded events at these landslides were triggered directly by rainfalls. Hence no long period precursors could be expected. For some triggering events, the data suggested that the pre-wetting of the subsurface (indicated by a smooth resistivity decrease initiated 4–8 days in advance for the test site Ampflwang) also played an important role in triggering a landslide. The monitoring results showed that all events were accompanied by a significant decrease in resistivity. The resistivity decrease preceded the triggering of the landslide by 11 (Bagnaschino) and 20–36 hours (Ampflwang). Consequently, a measuring interval of 6 hours seems to be too long to derive a well-defined trend evaluation during 'on time' data analysis before a triggering event. Therefore, if apparent resistivity should be used as an additional early-warning parameter, a much shorter measuring interval (0.5–1 hour) has to be applied to enhance the reliability of the trend prediction.

The study also showed that the geometrical analysis of the geoelectrical monitoring results, derived from an innovative 4D resistivity inversion approach, gave clear indications of possible processes responsible for the final triggering of the slide (i.e. the penetration of the wetting front down to a certain depth in the case of the Hausruck test site and the achievement of a certain degree of saturation of a basin-like subsurface structure in the case of the Bagnaschino test site). On the basis of the experiences gained from the investigated test sites, it might be possible to evaluate future critical situations by means of apparent resistivity monitoring, but it is almost impossible to exactly predict a sliding event. However, for this purpose, the processing of geoelectrical monitoring data with complex 4D algorithms is necessary. With current technical and financial means, this is difficult to be performed on a daily basis.

The results from both test sites demonstrated the usefulness of permanent automatic displacement monitoring for early-warning purposes. However, they also highlight the necessity to accompany these displacement measurements (which provide only point information) by monitoring of other parameters (especially water level and geoelectrics), since especially geoelectrical monitoring, due to its pre-eminently high spatial resolution, can definitely help to extrapolate the results of local displacement monitoring to a cross section of the subsurface. Otherwise, a reliable interpretation of displacement results and an assessment of possible further impacts, especially for early-warning purposes, are very difficult. On the other hand, this study also shows that the interpretation of resistivity (monitoring) data, if targeted at

the detection of underlying triggering processes, is significantly more reliable if combined with additional monitoring data, like displacement, precipitation and water levels at a high temporal resolution (sampling rate at least every half hour).

Hence, we conclude that resistivity monitoring very efficiently supplements automatic displacement measurements by providing wide-area knowledge with a high spatial resolution about ongoing subsurface processes, and therefore it could efficiently support decision-making in the case of emergencies.

ACKNOWLEDGEMENTS

The geoelectrical monitoring is supported by the project 'TEMPEL – Temporal changes of geoelectrical properties as possible indicator of future failure of high risk landslides' funded by the Federal Ministry for Transport, Innovation and Technology and the Austrian Science Fund (FWF): TRP 175-N21 in the frame of the Translational Brainpower Program, the FP7 project 'SafeLand – Living with the landslide risk in Europe' and by internal funds of the Geological Survey of Austria. The fourth author acknowledges the Basic Research Projects of the KIGAM that allowed him to conduct his research. We would like to thank Faletto Corrado for geological support at the test site Bagnaschino and the Provincia di Cuneo for making the D.M.S. and precipitation data available to the project and financially supporting the field installation procedure. We further acknowledge the support of G. Moser for selection of the site of Ampflwang and geological counselling and R. Potzmann, Central Institute for Meteorology and Geodynamics (ZAMG) for allocating the meteorological data from the station Wolfsegg i. Hausruck. We would also like to thank the family Gaisbauer, owner of the endangered house in Ampflwang, for their support at the test site Ampflwang, SFC Smart Fuel Cell AG for providing a test fuel cell EFOYPro for the Bagnaschino site and KTS GesmbH/Mr. Sporrer for supporting the maintenance of the combined solar-fuel cell power supply. We would like to thank David Gunn and another anonymous reviewer, whose comments significantly improved the quality of the paper.

REFERENCES

Archie G.E. 1942. The electrical resistivity log as an aid in determining some reservoir characteristics. *Petroleum Transaction of AIME* **146**, 54–62.

Atkins E.R. and Smith G.H. 1961. The significance of particle shape in formation factor-porosity relationships. *Journal of Petroleum Technology* **13**(3), 285–291.

Baron I. and Supper R. 2010. A general assessment of landslide investigation and monitoring methods in Europe (preliminary results). In: *Monitoring Technologies and Early Warning Systems – Current Research and Perspectives for the Future*, (eds R. Supper and I. Baron). Book of extended abstracts, Open Workshop in frame of the EU FP7 "Safeland" Project, February 24th, Vienna. Berichte der Geologischen Bundesanstalt 82, Vienna.

Bell R., Thiebes B., Glade T., Becker R., Kuhlmann H., Schauerte W. *et al.* 2008. The technical concept within the Integrative Landslide Early Warning System (ILEWS). In: *Geotechnologien* – Science Report 14.

Chacón J., Irigaray C., Fernández T. and El Hamdouni R. 2006. Engineering geology maps: Landslides and geographical inforation systems. *Bulletin of Engineering Geology and the Environment* **65**(4), 341–411.

Chambers J.E., Meldrum P.I., Gunn D.A., Wilkinson P.B., Kuras O., Weller A.L. *et al.* 2009. Hydrogeophysical monitoring of landslide processes using automated time-lapse electrical resistivity tomography (ALERT) [extended abstract]. *Near Surface 2009*, Dublin, Ireland, 7–9 September.

Chambers J.E., Hobbs P., Pennington C., Jones L., Dixon N., Spriggs M. *et al.* 2010. Integrated LiDAR, geophysical and geotechnical monitoring of an active inland landslide, UK. *Geophysical Research Abstracts* **12**, EGU2010-5244.

Chambers J.E., Meldrum P.I., Gunn D.A., Wilkinson P.B., Merritt A., Murphy W. *et al.* 2011. Geophysical-geotechnical sensor networks for landslide monitoring. *Proceedings of the Second World Landslide Forum*, Rome, 3–7 October 2011.

Daily W., Ramirez A., Labrecque D. and Nitao J. 1992. Electrical-resistivity tomography of vadose water-movement. *Water Resources Research* **28**, 1429–1442.

Foglino L., Lovisolo M. and Della Giusta A. 2006. Contribution of D.M.S. monitoring systems in the analysis of slide micro-movements for early warning management, risk assessment and evaluation of mitigating actions. *Geophysical Research Abstracts* **8**, 06122.

Giuliani A., Bonetto S., Castagna S., Comina C. and Mandrone G. 2010: A Monitoring System for Mitigation Planning: The Case of "Bagnaschino" Landslide in Northern Italy. *American Journal of Environmental Sciences* **6**(6), 516–522.

Hayley K., Pidlisecky A. and Bentley L.R. 2011. Simultaneous time-lapse electrical resistivity inversion. *Journal of Applied Geophysics* **75**, 401–411.

Jackson P., Taylor-Smith D. and Stanford P.N. 1978. Resistivity-porosity-particle shape relationships for marine sands. *Geophysics* **43**(6), 1250–1268.

Jongmans D. and Garambois S. 2007. Geophysical investigation of landslides: a review. *Bulletin de la Societe Geologique de France* **178**(2), 101–112.

Karaoulis M.C., Kim J.-H. and Tsourlos P.I. 2011a. 4D active time constrained resistivity inversion. *Journal of Applied Geophysics* **73**, 25–34.

Karaoulis M., Revil A., Werkema D.D., Minsley B.J., Woodruff W.F. and Kemna A. 2011b. Time-lapse three-dimensional inversion of complex conductivity data using an active time constrained (ATC) approach. *Geophysical Journal International* **187**, 2237–251.

Karaoulis M., Revil A., Zhang J. and Werkema D.D. 2012. Time-lapse joint inversion of crosswell DC resistivity and seismic data: A numerical investigation. *Geophysics* **77**, D141–D157.

Kim J.-H., Yi M.-J., Park S.-G. and Kim J.G. 2009. 4-D inversion of DC resistivity monitoring data acquired over a dynamically changing earth model. *Journal of Applied Geophysics* **68**, 522– 532.

Kim J.-H., Yi M.-J., Ahn H.-Y. and Kim K.-S. 2010. 4-D Inversion of Resistivity Monitoring Data Using L1 Norm Minimization. *Proceedings of Near Surface 2010*, A15, Zurich, Swiss, 6–8 September.

Kim J.-H., Supper R., Tsourlos P. and Yi M.-J. 2012. 4D inversion of resistivity monitoring data through Lp norm minimizations. *Proceedings of Near Surface Geoscience 2012*, A24, Paris, France, 3–5 September.

Kim J.-H., Supper R., Tsourlos P. and Yi M.-J. 2013. Four-dimensional inversion of resistivity monitoring data through Lp norm minimizations. *Geophysical Journal International* (in review).

LaBrecque D.J. and Yang X. 2001. Difference inversion of ERT data: a fast inversion method for 3-D in situ monitoring. *Journal of Environmental and Engineering Geophysics* **6**, 83–89.

Lebourg T., Hernandez M., Zerathe S., El Bedoui S., Jomard H. and Fresia B. 2010. Landslides triggered factors analysed by time lapse

electrical survey and multidimensional statistical approach. *Engineering Geology* **114**(3–4), 238–250

Loke M.H. 1999. Time lapse resistivity imaging inversion. *Proceedings of the 5th Meeting of the EEGS European Section*, Em1.

Loke M.H., Dahlin T. and Rucker D.F. 2013. Smoothness-constrained time-lapse inversion of data from 3-D resistivity surveys. *Near Surface Geophysics* (in press).

Lovisolo M. 2011. Bagnaschino Landslide: From early warning to site-specific kinematic analysis. *Berichte der Geologischen Bundesanstalt* **82**, ISSN 1017–8880 – Landslide Monitoring Technologies & Early Warning Systems, Vienna.

Luongo R., Perrone A., Piscitelli S., and Lapenna V. 2012. A Prototype System for Time-Lapse Electrical Resistivity Tomographies. In: *Electrical Imaging for Geohazard and Environmental Monitoring*, (eds V. Lapenna, S. Piscitelli and P. Soupios). International Journal of Geophysics, Article ID 176895, 12 pages. doi:10.1155/2012/176895

Mauritsch H.J., Seiberl W., Arndt R., Römer A., Schneiderbauer K. and Sendlhofer G.P. 2000. Geophysical investigations of a large landslide in the Carnic Region (case study). *Engineering Geology* **56**, 373–388.

Meric O., Garambois S., Jongmans D., Wathelet M., Chatelain J.-L. and Vengeon J.-M. 2005. Application of geophysical methods for the investigation of the large gravitational mass movement of Séchilienne, France. *Canadian Geotechnical Journal* **42**, 1105–1115.

Miller C.R., Routh P., Brosten T. and McNamara J. 2008. Application of time-lapse ERT imaging to watershed characterization. *Geophysics* **73**, 7–17.

Oldenborger G.A., Knoll M.D., Routh P.S. and LaBrecque D.J. 2007. Time-lapse ERT monitoring of an injection/withdrawal experiment in a shallow unconfined aquifer. *Geophysics* **72**, 177–187.

Peisino V., Pepe M., Brunamonte F. and Belloma A. 2009a. Movimento Franosa in Localita Bagnaschino, Valutazione geologica e geotecnica del movimento franoso sulla SP. 164 e definizione a livello di studio di fattibilità degli interventi tecnici da adottare, Fase 1 Step conoscitivo generale, Ingegneria Geotecnica, Torino, Italy.

Peisino V., Brunamonte F., Lampone G.F. and Belloma A. 2009b. Movimento Franosa in Localita Bagnaschino, Valutazione geologica e geotecnica del movimento franoso sulla SP. 164 e definizione a livello di studio di fattibilità degli interventi tecnici da adottare, Fase 2 - Campagna geognostica integrativa R 2.1 - Relazione sulle indagini geognostiche e geofisiche, Ingegneria Geotecnica, Torino, Italy.

Peisino V., Brunamonte F., Lampone G.F. and Belloma A. 2009c. Movimento Franosa in Localita Bagnaschino, Valutazione geologica e geotecnica del movimento franoso sulla SP. 164 e definizione a livello di studio di fattibilità degli interventi tecnici da adottare, Fase 3 Monitoraggio di superficie e di sottosuolo, R 3.1 – Risultati acquisiti con le attività di monitoraggio del versante, Ingegneria Geotecnica, Torino, Italy.

Perrone A. 2001. Electrical and Self-Potential tomographic techniques for landslide monitoring: first results on Southern Apennine Chain (Italy). II international Workshop on Geo-Electro-Magnetism / Abstract, Memorie dell'Accademia Lunigianese di Scienze "G. Capellini" Vol. LXXI (2001), Scienze Matematiche, Fisiche e Naturali, La Spezia.

Perrone A., Iannuzzi A., Lapenna V., Lorenzo P., Piscitelli S., Rizzo E. *et al.* 2004. Highresolution electrical imaging of the Varco d'Izzo earthflow (southern Italy). *Journal of Applied Geophysics* **56**, 17–29.

Perrone A., Zeni G., Piscitelli S., Pepe A., Loperte A., Lapenna V. and Lanari R. 2006. Joint analysis of SAR interferometry and electrical resistivity tomography surveys for investigationg ground deformation: the case-study of Satriano di Lucania (Potenza, Italy). *Engineering Geology* **88**, 260–273.

Rucker D.F., Finka J.B. and Loke M.H. 2011. Environmental monitoring of leaks using timelapsed long electrode electrical resistivity. *Journal of Applied Geophysics* **74**, 242–254.

Schlumberger 1987. Log Interpretation Charts, Houston, Schlumberger Educational Services.

Supper R., Hübl G. and Jaritz W. 2002. Geophysical Surveys for the investigation and monitoring of landslide areas. *Proceedings of the Environmental and Engineering Geophysical Society, 8th Meeting Aveiro*, Portugal.

Supper R., Ahl A., Römer A., Jochum B. and Bieber G. 2008. A complex geo-scientific strategy for landslide hazard mitigation – from airborne mapping to ground monitoring. *Advances in Geosciences* **14**, 1–6.

Supper R., Römer A. and Jochum B. 2009. Geoelectrical measurements for natural hazard monitoring. *SEGJ 9th International Symposium*, Extended Abstracts, Sapporo.

Supper R., Baron I., Jochum B., Ita A., Winkler E., Motschka K. and Moser G. 2010. From structural investigation towards multi-parameter early warning systems: geophysical contributions to hazard mitigation at the landslide of Gschliefgraben (Gmunden, Upper Austria), *Geophysical Research Abstracts* **12**, EGU2010-4649-1.

Supper R., Jochum B., Ottowitz D., Baroň I., Vecchiotti V., Pfeiler S. *et al.* 2012a. Case histories – Analysis of real monitoring data: Bagnaschino. In: *The Safeland Project, Deliverable 4.6, Report on evaluation of mass movement indicators*, (eds L. Baron and R. Supper), Vienna, 191–220.

Supper R., Jochum B., Baroň I., Ottowitz D., Pfeiler S., Römer A. *et al.* 2012b. Case histories – Analysis of real monitoring data: Ampflwang-Hausruck. In: *The Safeland Project, Deliverable 4.6, Report on evaluation of mass movement indicators*, (eds L. Baron and R. Supper), Vienna, 150–173.

Wilkinson P.B., Chambers J.E., Meldrum P.I., Gunn D.A., Ogilvy R.D. and Kuras O. 2010. Predicting the movements of permanently installed electrodes on an active landslide using time-lapse geoelectrical resistivity data only. *Geophysical Journal International* **183**(2), 543–556.

Winsauer W.O., Shearin H.M., Jr., Masson P.H. and Williams M. 1952. Resistivity of brine saturated sands in relation to pore geometry. *AAPG Bulletin* **36**, 253–277.